Block Island Offshore Wind Farm

Collision monitoring

MUSE Report – Analyses of radar and camera data 2018-2022

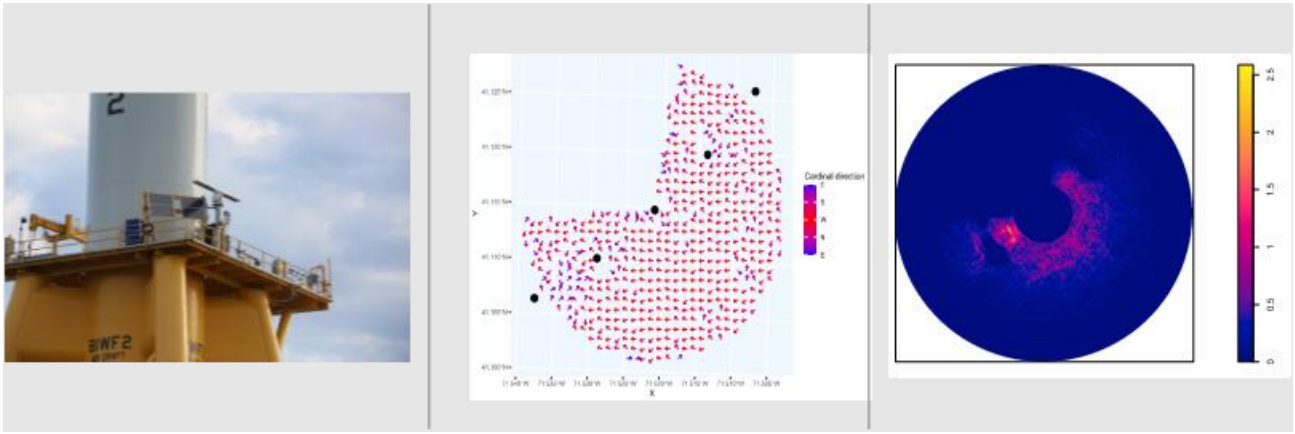

July 11, 2024

Prepared for Ørsted

Block Island Offshore Wind Farm

MUSE Report – Analyses of radar and camera data 2018-2022

Prepared for: Ørsted
Represented by Kimberly Peters

Contact person:	Henrik Skov, hsk@dhigroup.com
Project Manager:	Henrik Skov
Quality Supervisor:	Rien van Wijk
Author:	Henrik Skov, Maans Karlsson
Project No.:	41803580-1
Approved by:	Rien van Wijk
Approval date:	31 May 2024
Revision:	Final 3.0
Classification:	**Confidential:** This document is only accessible to the project team members and sharing it outside the project team is subject to the client's prior approval. Photos Thomas W. Johansen
File name:	DHI_MUSE_Block Island_Bird monitoring results 2018-2021_KIPET_BRIWO_JEFWE_jlc_DHI Revisions.docx

Contents

Figures

Tables

1 Introduction

The Block Island Wind Farm (BIWF; Project), owned by Deepwater Wind Block Island, LLC (Deepwater Wind), is located approximately 4.8 kilometers (km; 3 miles [mi]) southeast of the coast of Block Island, Rhode Island (Figure 1-1). Block Island is an approximately 27.0 square km (10.4 square mi) island located approximately 14.9 km (9.3 mi) south of the Rhode Island mainland and 21.9 km (13.6 mi) northeast of the tip of Long Island, New York. The 30-megawatt (MW) BIWF consists of five General Electric (GE) Haliade 150 6-MW wind turbine generators (WTGs) and a submarine inter-array cable and export cable, which connects the BIWF to a substation on Block Island. The BIWF began commercial operations in December 2016. The maximum rotor-swept height of the BIWF WTGs is 180 meters (m; 591 feet [ft]) above water level. The turbines are spaced approximately 0.4 nautical miles (nm; 0.5 miles [mi]) apart.

Post-construction avian and bat surveys were required as a condition of the United States Army Corps of Engineers and the Rhode Island Coastal Resources Management Council permits issued for construction of the Project, as outlined in the Project's Construction and Post-Construction Avian and Bat Monitoring Plan (revised April 2015 PCMP; Tetra Tech 2015). Deepwater Wind selected DHI Water and Environment (DHI) as a sub-consultant to deploy their MUltiSEnsor remote wildlife detection system (MUSE). Deepwater Wind contracted Stantec Consulting Services Inc. (Stantec) to provide Project oversight and to collaborate with DHI on data analysis and data summary.

Post-construction monitoring studies were initiated at the Project in January 2017 after the Project was commissioned. The MUSE system was deployed to monitor bird and bat activity in the vicinity of BIWF turbines and record video footage of potential bird/bat-wind turbine interactions. The turbine platform mounted MUSE system is designed to monitor, via radar, the airspace around the two turbines (Turbines 1 and 3) which are distanced approximately 0.4 nm from the turbine on which it was deployed (Turbine 2). The radar triggers a bank of three video cameras (two thermal and one daylight) to track detected targets near those two adjacent turbines.

The MUSE system is a relatively new technology that DHI has continued to develop as the study progressed. The PCMP specified deployment of the MUSE system in January 2017, after project commissioning, with monitoring originally planned to occur in 2017, 2019, and 2021 (Years 1, 3, and 5, respectively).

However, due to a series of administrative and logistical delays involving turbine and cable access, adverse weather, and equipment mobilization, initial deployment of the MUSE system on Turbine 2 occurred in May 2017 and operational status was not achieved until October 2017. Due to the delay in operational status in 2017, the system was deployed continuously until May 2021, instead of operating the system only every second year as originally planned. The system is designed to be continuously running and, in fact, functions better if long-term shutdowns are avoided.

This final report on the monitoring results covers the entire monitoring period, an approximate 34-month period from August 1, 2018 to May 13, 2021 when the system was operating successfully. However, the focus of the analyses of the radar data for this report is on the period from January 1, 2019 to May 13,

2021 (intensive sampling period) for which DHI adjusted the radar analysis software to apply high-frequency sampling of radar screen images.

The objectives of this report were to summarize all the recorded radar tracks during the period of intensive sampling (January 1, 2019 to May 13, 2021) and the radar tracks with associated video files for the operational monitoring period (August 1, 2018 to May 13, 2021). The latter focused on video files recorded within approximately 100 m (328 ft) of Turbines 1 and 3, specifically to describe potential micro avoidance (response to avoid approaching within 10 m of the turbine rotor [Skov et al. 2018]) or any potential collision events.

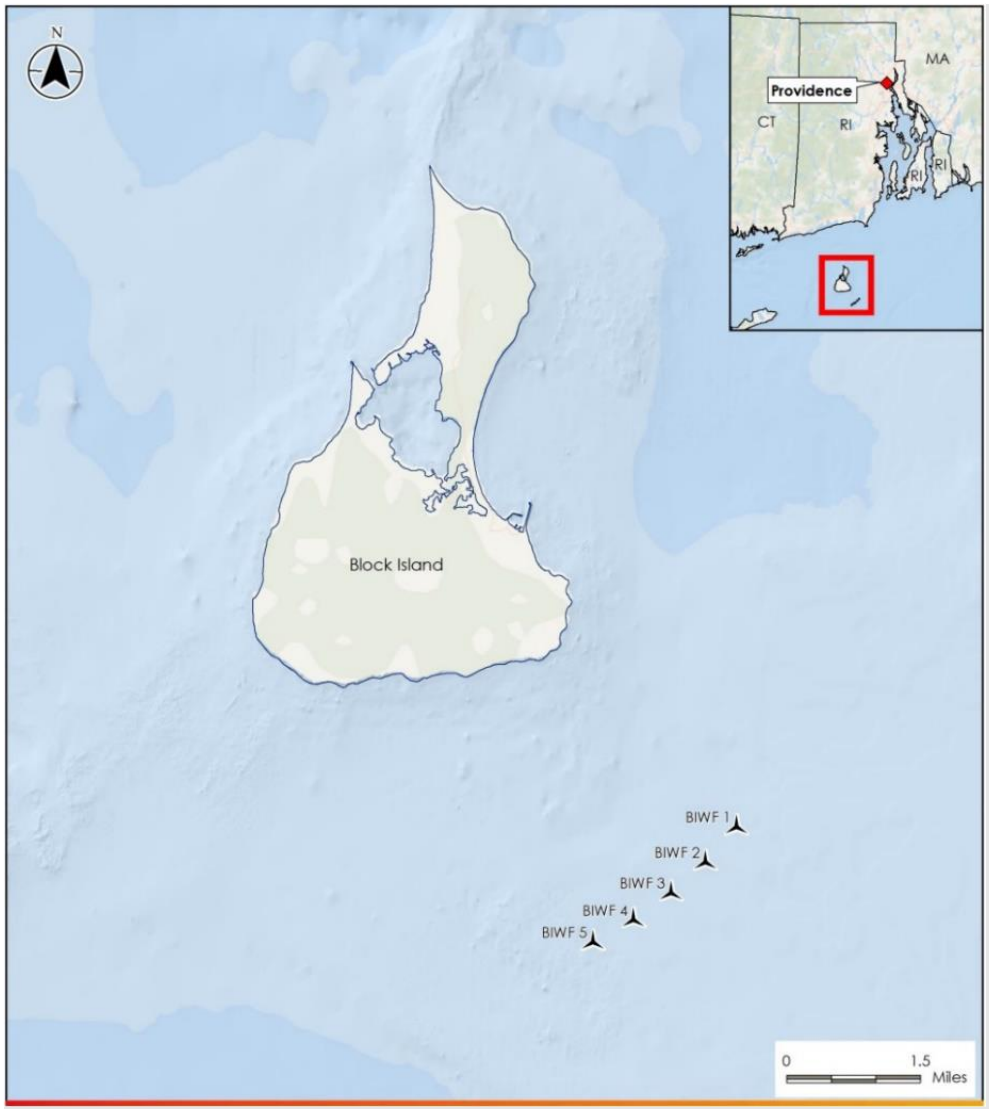

Figure 1-1 Block Island Wind Farm, Rhode Island

2 The MUSE system

DHI's MUSE system is a combination of a Furuno® FAR3000 S-band radar (with enhanced sea clutter suppression) and Voyager III pan-tilt zoom digital (thermal-visual) camera. The system consists of a weatherproof camera housing with two thermal night vision cameras and a dual-function zoom daylight/lowlight color TV camera. The camera, with a 26X optical zoom and 15X (thermal)/312X (visual) digital zoom, was designed to respond immediately to the coordinated information transferred from the radar. The radar antenna measures 12 ft and uses a frequency of 3050 MHz and an output power of 250 W.

The system was programmed to only track bird targets when they were detected within 1,500 m of the radar system (radar swept zone). When operating successfully and when a target (e.g., bird) is detected within that distance, the coordinates are transmitted from the radar to the camera, which then begins tracking the target in tandem with the radar. To facilitate smooth data transfer between radar and camera, the radar bird tracking software tracks at a rate of 24 times per minute. In addition, the camera software enables target selection based on the tracking data from the radar.

The radar scans continuously for targets within the radar swept zone from the Turbine 2 platform and will follow a target until it has not been recorded for a defined period (e.g., for two antenna rotations). The camera works in defined time steps (e.g., 40 seconds). Once it receives information about a target from the radar, the camera focuses on the radar target until the radar loses the target or a new recording of the target is initiated. Radar tracks are continuously recorded to a geo-database by the system where associated images from the camera are also stored.

The digital communication is controlled by the MUSE software for automated tracking and geo-referencing of species-specific track data and for storage of recorded tracks and videos. The software also controls the filtering of static and dynamic noise and tracking of bird and bat targets. After filtering static noise from the BIWF infrastructures and dynamic noise from waves and precipitation, the radar data are processed by extracting moving targets from the radar images sampled for each 2.5 secs rotation of the antenna.

A target detection calibration was conducted in September 2018. The calibration included deployment of three variably sized unmanned aerial vehicles (drones), sequentially operated from the stern of the support vessel Lindsey E, in the vicinity of BIWF Turbine 3. The smallest drone was intended to mimic the size of a medium-sized passerine or large bat. The radar tracking successfully documented drone activity in the airspace around Turbine 3 (within 100 m). Hence, it is assumed that the MUSE system fully covered the sea area between Turbines 1, 2 and 3.

Figure 2-1 DHI's MUSE wildlife detection system deployed on Turbine 2

3 Collected data

The MUSE system was originally scheduled to begin operations in January 2017, following the successful commissioning of BIWF; however, a series of administrative and logistical delays involving turbine and cable access, adverse weather, and equipment mobilization delayed initial deployment on Turbine 2 until May 2017. The system was subsequently hampered by a series of technical constraints, including power losses and overheating, which resulted in a shutdown and redesign of the equipment housing. A system retrofit was conducted and the system became operational in early October 2017. Due to the delay in operational status in 2017, the system was left to operate continuously until May 13, 2021.

Note that this report summarizes all the recorded radar tracks during the period of intensive sampling (January 1, 2019 to May 13, 2021) and the radar tracks with associated video files for the operational monitoring period (August 1, 2018 to May 13, 2021).

From August 1, 2018, to May 13, 2021 (an approximate 34 month and 1003-day period), the radar and video camera operated during 841 dates and 733 dates, respectively, and 20,184 hours and 17,592 hours, respectively, of 24,072 total hours during this timeframe (Table 3-1). Operational status of both MUSE components overlapped on 497 of these dates. Operational downtime periods were due to an initial issue with equipment overheating and then intermittent power losses. Otherwise, the MUSE system operated during both daytime and nighttime periods, during all weather conditions.

Table 3-1 Table 1. Operational success of MUSE radar and video camera, August 1, 2018, to May 13, 2021

Total No. Dates	Total No. Hours	No. Dates Radar Operated	No. Hours Operation Radar	No. Dates Camera Operated	No. Hours Operation Camera
1,003	24,072	841	20,184	733	17,592

The detailed analyses of radar tracks recorded between January 1, 2019 and May 13, 2021 (intensive sampling period for which DHI adjusted the radar analysis software to apply high-frequency sampling of radar screen images) were undertaken based on an improved tracking algorithm. DHI adjusted the radar analysis software to apply high-frequency sampling of radar screen images of tracks recorded during this timeframe (one radar screen image downloaded every 2 secs). A monthly breakdown of the number of radar screen frames is shown in Figure 3-1.

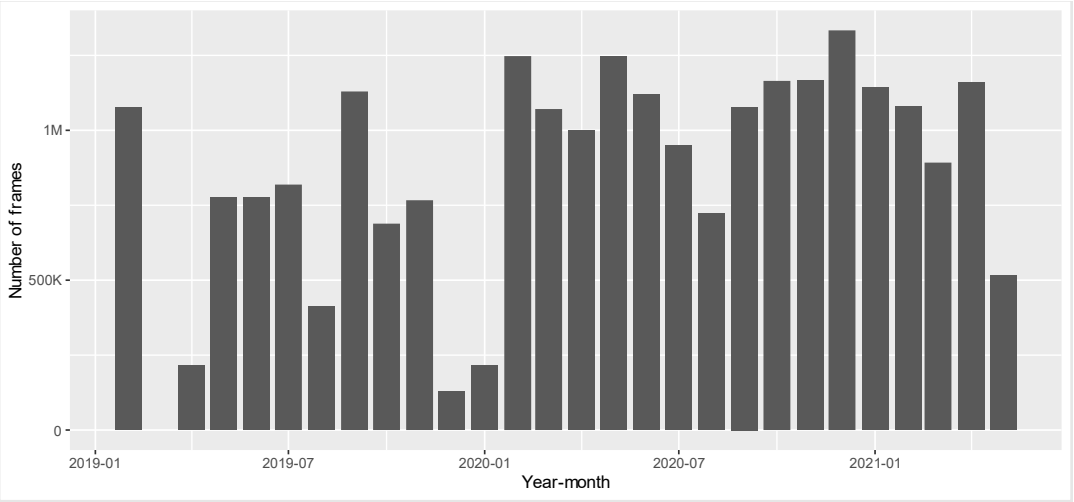

Figure 3-1 Daily number of radar screen images collected per month by the radar equipment during the period January 2019 through May 2021

4 Data analysis

The detailed analysis of the radar data included filtering the data for tracks that were assessed to likely be birds. Problems with false positives are common in autonomous radar data, see e.g. van Erp, Jens A et.al. (2023). Remaining tracks were used to estimate track length density in the radar swept zone (the scanned 1,500 m radius around the radar). These estimates are highly likely biased by the masking of the tracker that process the radar images and by the distance to the radar. These biases were accounted for as discussed in in the Biases section 4.7.

4.1 Track filtering

The raw data consisted of screenshots of the radar screen every 2 seconds. These were processed by DHI proprietary software to generate a dataset of tracks. The tracks were filtered in three ways to reduce the number of false positives: first we excluded all tracks that didn't have a reasonable enough change in distance to the radar during the duration of the track. Then we excluded tracks that contained nodes (nodes are the points a track is interpolated between) that were judged unreasonably common in the data. Finally, we excluded all tracks containing less than 10 nodes.

4.2 Track length density

Track length density is defined as track length per area unit, and plotted in a grid where each pixel corresponds to an area of 3.75 m x 3.75 m. As opposed to track count, this density will not inflate due to many tracks intersecting corners or edges of the pixels, but stay proportional to the amount of distance travelled by a track within each pixel. Mathematically, partition the radar swept zone Ω into D mutually disjoint blocks B_i, with $\cup_{i=1}^{D} B_i = \Omega$. Then let N be the number of tracks and denote track j with $t_j, j = 1, \dots, N$. Denote whether t_j passes through b_i with $1(t_j \cap b_i)$, and denote the length of t_j that lies within b_i by $l(t_j \cap b_i)$. For any block B_i, the track length density

$$\varphi_i = \frac{\sum_{\{j:1(t_j \cap b_i)=1\}} l(t_j \cap b_i)}{A(b_i)}$$

where $A(b_i)$ is the area of b_i. We have chosen to partition Ω in equally sized and shaped areas, so $A(b_i) \equiv a$.

This is a central measure of bird activity within the radar swept zone. The smaller we choose the pixel size to be (as measured in real world distances), the higher resolution we get in the track length density.

4.3 Flight directions

For each node except the last in a track, the travelling direction can be estimated with basic trigonometric calculations. For each track, the mean direction of the track is computed by calculating the circular mean of the travelling directions between nodes in the track. These mean track directions are then used to create the directional histograms showing mean directions in relation to true north.

4.4 Local track directions

The local track directions use the directions estimated for nodes within a track, to capture changes in flight direction during the track. In short, the radar swept zone is partitioned into disjoint areas and within each area the circular mean of all track directions is computed. The mean value is then plotted as an arrow for which points in the average travel direction of tracks in that area.

4.5 Track length density as a function of distance to rotor

With the track length density estimated for the radar swept zone, we can choose any point within the radar swept zone and see what the track length density is at that point. We can also choose a location and check the track length density along a line in an arbitrarily chosen direction. This forms the basis for estimating the track length density as a function of distance to the rotor. We choose the location of Turbine 1 or 3, and then check the track length density in 360 directions uniformly distributed over the cardinal directions. The density is checked from the chosen location up to 666 m from the turbine, and the track length density is estimated as a smooth function of distance from the turbine rotor.

4.6 Biases

4.6.1 Target differentiation

As the spatial resolution in the FAR-3000 radar is rather coarse (approximately 25 m) the detected tracks may represent several individuals or flocks of birds. The quantification of track density may therefore not be used as a proxy for the density of individual birds, but rather as an index of activity within the radar swept zone.

4.6.2 Masking

The strongest biases are likely those created by the masking of the track scanner. The scanner ignores regions of the radar screen that it is configured to consider as clutter. In Figure 4-1 an example of a mask can be seen. The mask is updated regularly, and based on the mask, average masks can be computed. Figure 4-1 contains the average mask for May 2020. The black areas are always masked, and the lighter an area is, the less often it has been masked. No attempt was made to process track data within the masked areas. No scanning was performed between W and N, as it was hidden from the radar by the turbine tower this area should thus be ignored when looking at the mask.

As can be seen, Turbines 1 and 3 were completely masked (completely black) from the radar view during the study period, and thus we cannot say anything about the radar track activity in the rotor-swept zones of these turbines. Any estimates within 75 m from a turbine should be interpreted with caution due to the masking effect. Thus the summary of micro avoidance behavior focused on video files recorded within approximately 100 m (328 ft) of Turbines 1 and 3 (instead of radar tracks).

4.6.3 Distance from radar

Radars detect objects based on the energy the object reflects back to the radar. The more energy the object reflects, the larger cross section area the object is said to have. The size, shape, material and angles of the surfaces of the object all influence the cross-sectional area.

In general, the further away an object of fixed cross-sectional area is, the less likely it is to be detected by the radar. This can lead to biases in the estimation of track length density, since birds might not be detected by the radar at further distances, or only be detected during a minority of the sweeps it is within the radar swept zone, causing fragmented tracks. This so-called distance bias has been evaluated for the FAR-3000 radar using theoretical detection curves for different sizes of birds (radar cross-sections) computed by the Carpet simulation software https://www.tno.nl/en/safe/information-sensor-systems/carpet-computer-aided-radar-performance/ (Appendix A). The detection curves within the radar swept zone applied in BIWF shows good and even detection of both large birds like Northern Gannets (*Morus bassanus*), medium-sized birds like Herring Gulls (*Larus argentatus*) and small birds like songbirds throughout the range. Hence, the distance bias at BIWF was judged as minimal.

4.6.1 Impact of dynamic clutter filters

The radar software applies dynamic clutter filters to remove noise imposed by rain and waves. These filters efficiently dampen the background scatter created by rain and waves. During calm, dry periods echoes from birds are easily distinguishable from background scatter, yet during periods of heavy rain and high waves the background scatter will increase to the energy levels of birds which means that distinguishable reflections made by birds will be dampened or lost. As a result, during such weather situations false negative detections are evident with this radar. However, as all flight statistics extracted from the radar data integrate flight behavior data (e.g., avoidance of turbines) collected during the same weather conditions the false negative detections are unlikely to lead to significant spatial bias (same bias throughout radar range). The weather conditions during which the radar is judged as collecting unbiased bird data are sea states below Beaufort Sea State 5.

Figure 4-1 Radar mask. Images shows the mean level of masking during the month of May 2020. The intensity of black color reflects the frequency of masking during this month.

5 Results

5.1 Temporal dynamics of recorded density patterns

The phenological patterns of the collected radar bird tracks are depicted in Figure 5-1 through Figure 5-6. Figure 5-1 shows the average number of bird tracks per minute and indicates a lot of variation in bird activity over the monitored period, but with the month of July as the peak month in both 2019 and 2020. Videos collected during July 2019 and 2020 indicated a relatively high frequency of Great shearwaters (*Ardenna gravis*) and Cory's shearwaters (*Calonectris borealis*). A relatively high level of bird activity was also recorded in February 2019 dominated by Herring gulls, yet in all other winter months flight activity was relatively low. An increase in flight activity was noted in all three spring periods and, following the peak in July, activity levels remained high throughout fall.

The variation in recorded bird flight activity between day and night hours is shown in Figure 5-2, which indicates that the peak in the summer months is dominated by flight activity during daylight hours. During the main periods of seasonal migration of birds from the northern Hemisphere in April-May and August-November nocturnal flight activity was at least at the same level as daylight flight activity.

The daily variation in recorded bird tracks (Figure 5-3) displays a high degree of variation with prominent spikes of flight activity both during summer peak and winter and during spring and fall migration periods. Accordingly, the density of birds at BIWF should be expected to be highly variable during all times of the year in response to local feeding and migratory events.

An average hourly distribution of bird tracks is given in Figure 5-4 and the distribution seen in relation to sunrise and sunset are given in Figure 5-5 and Figure 5-6, respectively. These plots show highest overall flight activity during morning hours and lowest overall flight activity during late afternoon hours.

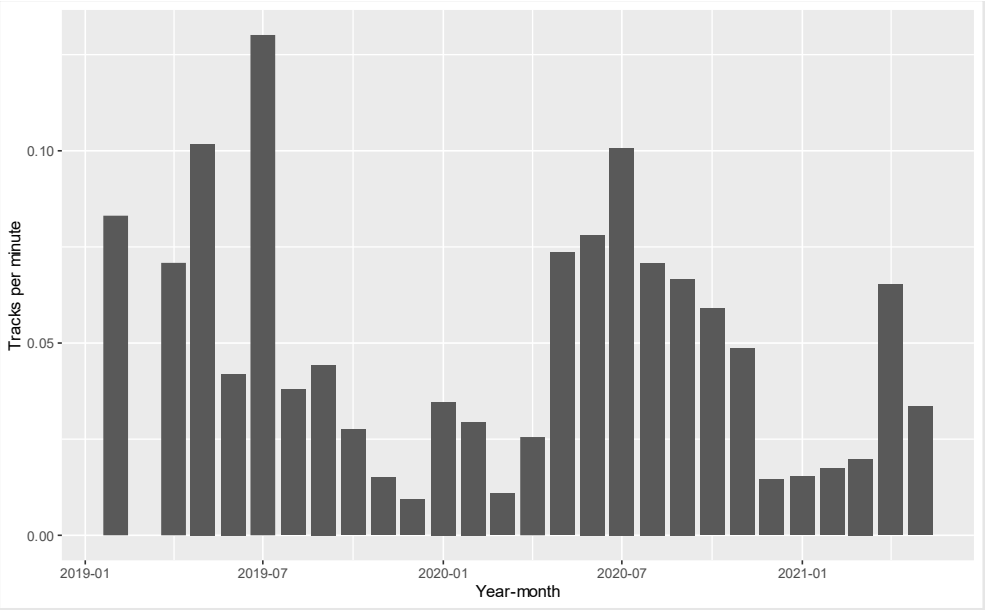

Figure 5-1 The number of radar bird tracks per minute per month for the period January 2019 – May 2021

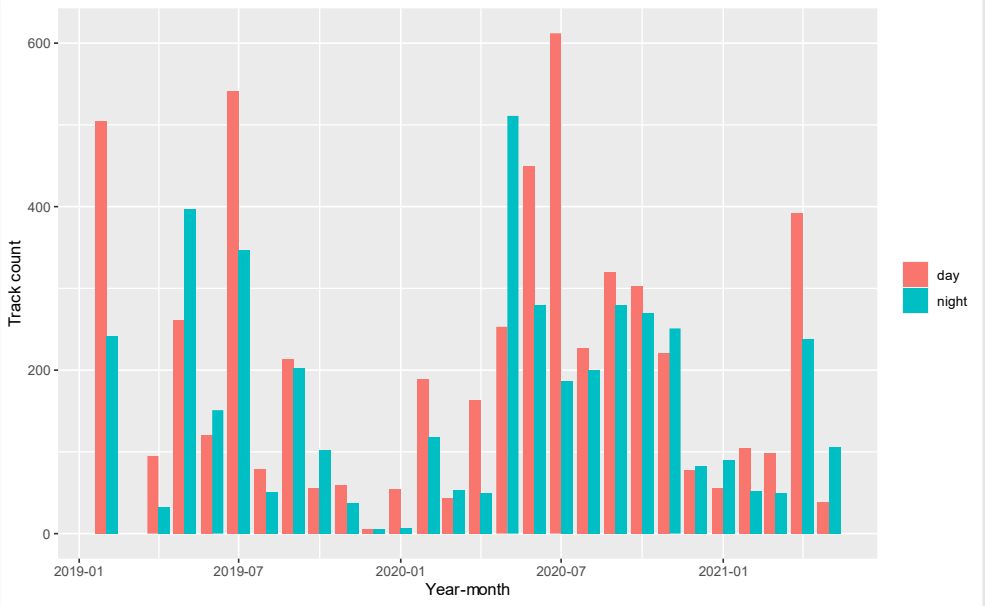

Figure 5-2 The total number of radar bird tracks per month split by day and night for the period January 2019 – May 2021

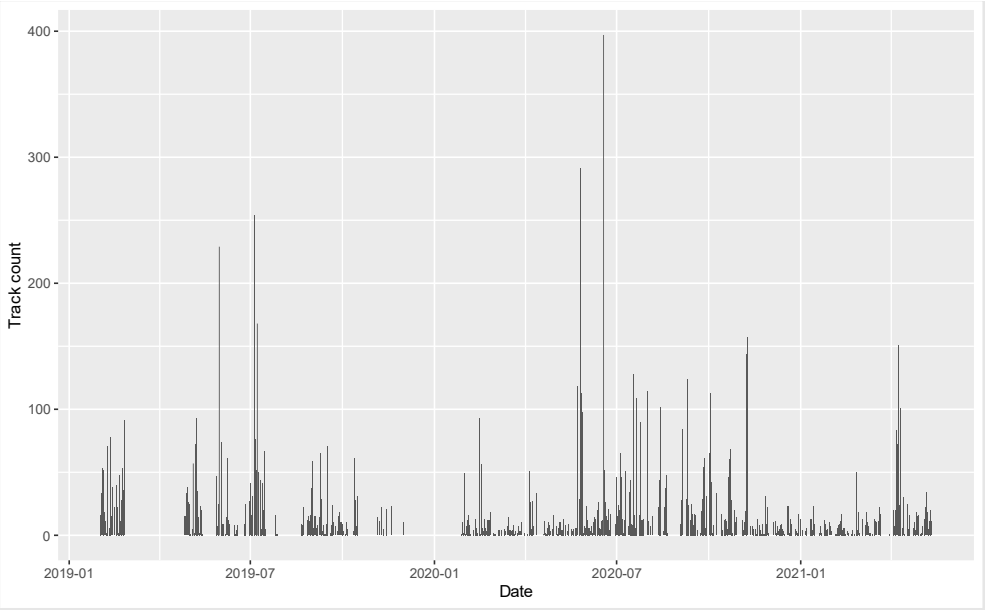

Figure 5-3 The total number of radar bird tracks per day for the period January 2019 – May 2021

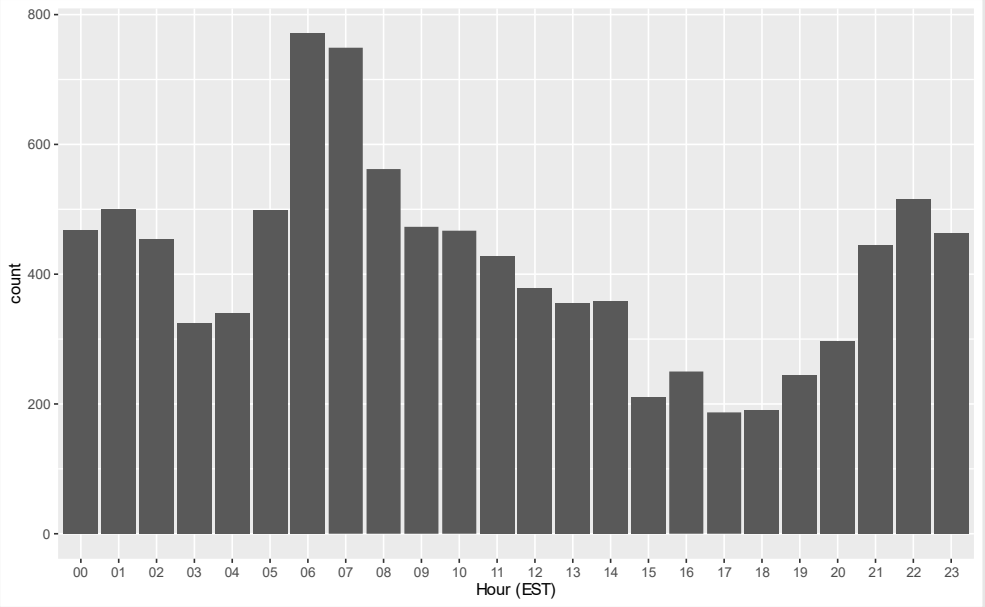

Figure 5-4 The total number of radar bird tracks per hour for the period January 2019 – May 2021

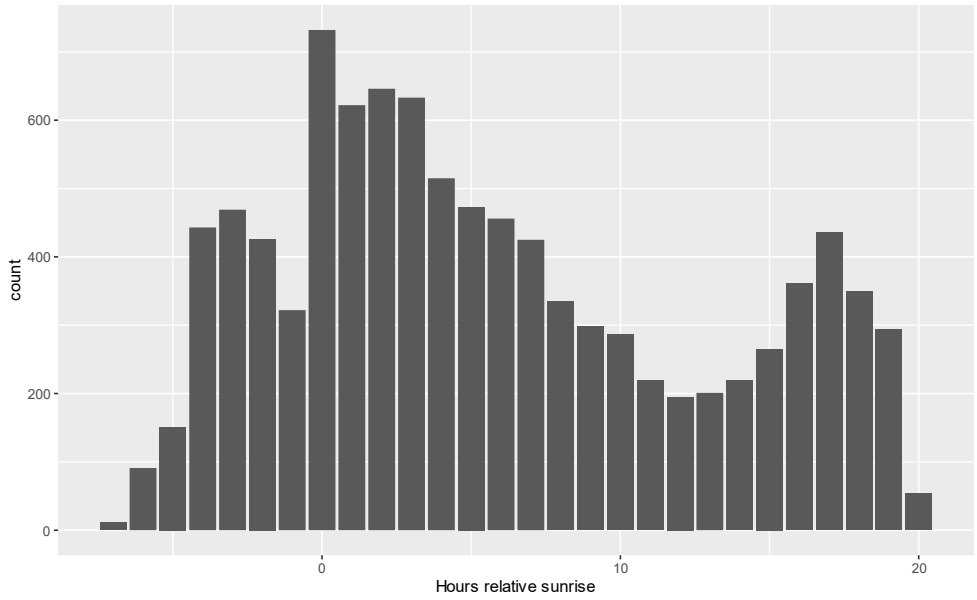

Figure 5-5 The total number of radar bird tracks per hour relative sunrise for the period January 2019 – May 2021

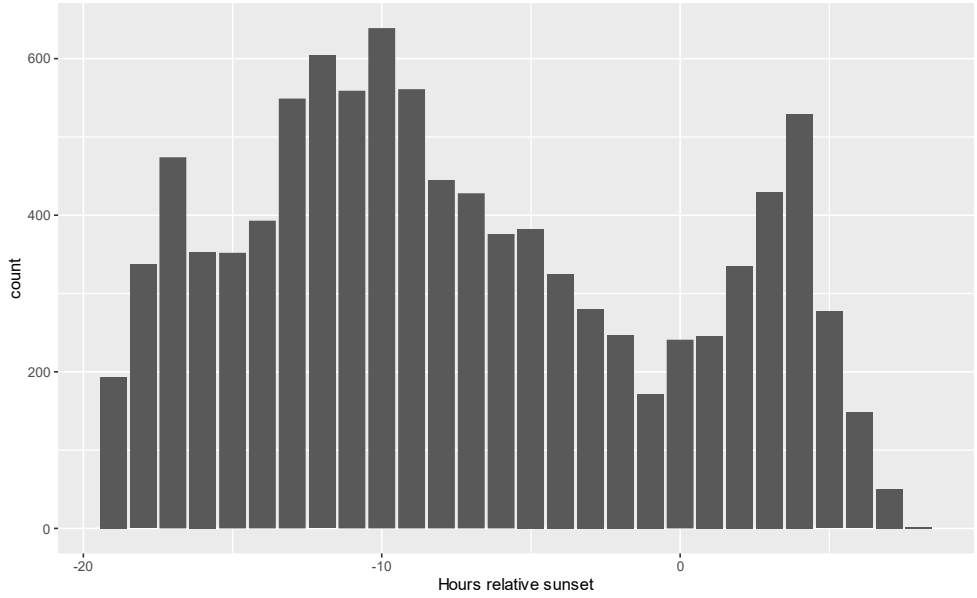

Figure 5-6 The total number of radar bird tracks per hour relative sunset for the period January 2019 – May 2021

5.2 Spatial dynamics of recorded density patterns

5.2.1 Daytime

A monthly breakdown of the spatial distribution and density of all recorded bird tracks (regardless of track length) during daylight hours is shown in Figure 5-7. The recorded patterns of flight distributions in all months clearly indicate avoidance of the turbines. This is so, even if the radar is shaded within the nearest 75 m from the turbine tower due to the static clutter induced by the

turbine and rotor blades. The zone of avoidance seems to stretch at least to 1/3 of the inter-turbine distance equivalent to 275 m. The general avoidance behaviour also clearly translates into a zone of higher densities located between the turbines and at 300-400 m distance along the array; that is, close to the mid-point between adjacent pairs of turbines.

Smaller scale flight patterns embedded in the spatial distributions during daylight hours are quite complex which may be due to a dominance of local-feeding seabirds. However, a tendency to circular movements is noticed close to turbine 1 and 3.

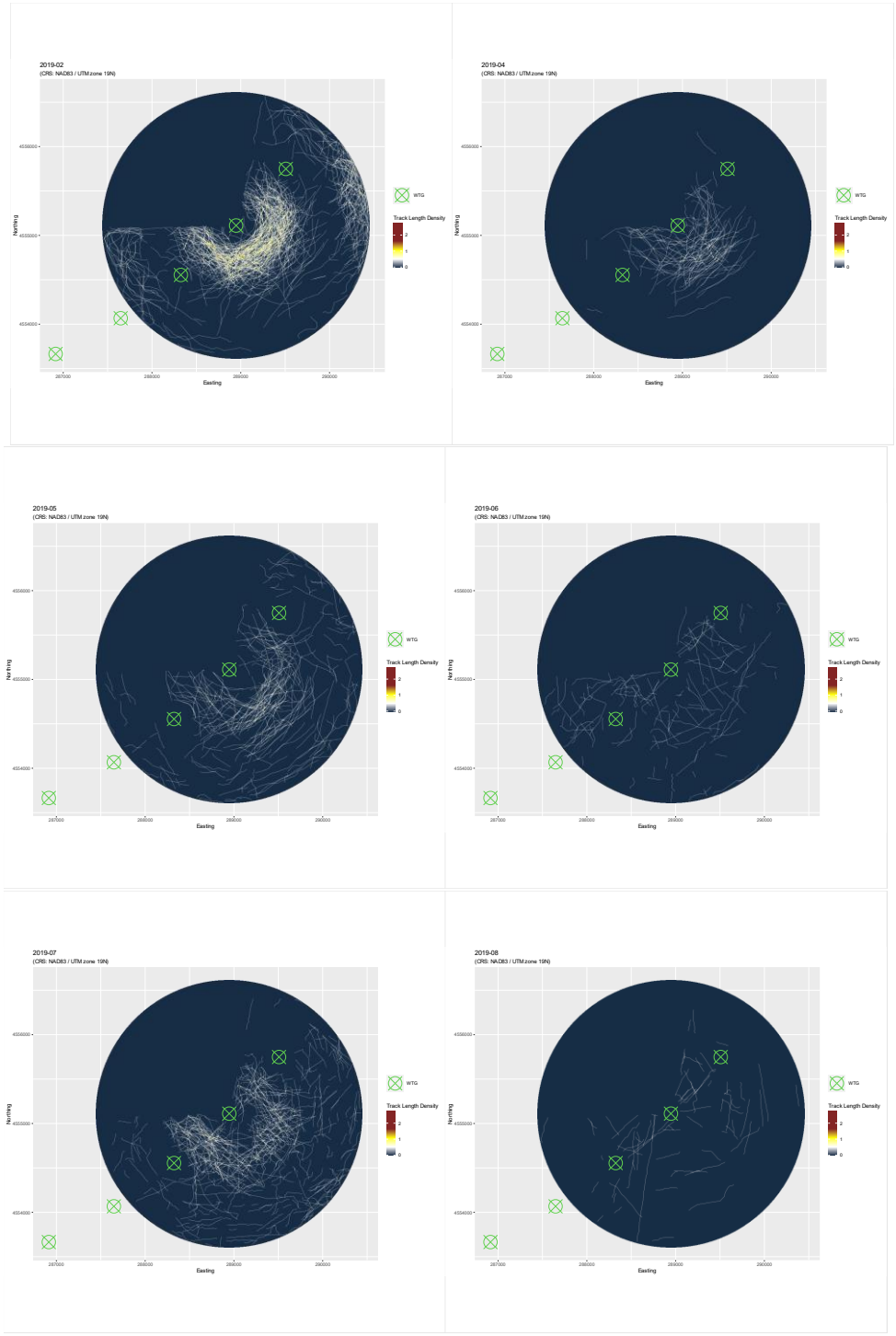

Figure 5-7 Monthly track length density patterns recorded during daylight hours by the radar during the period January 2019 – May 2021. The masked areas of the rotor-swept zones are marked by green circles.

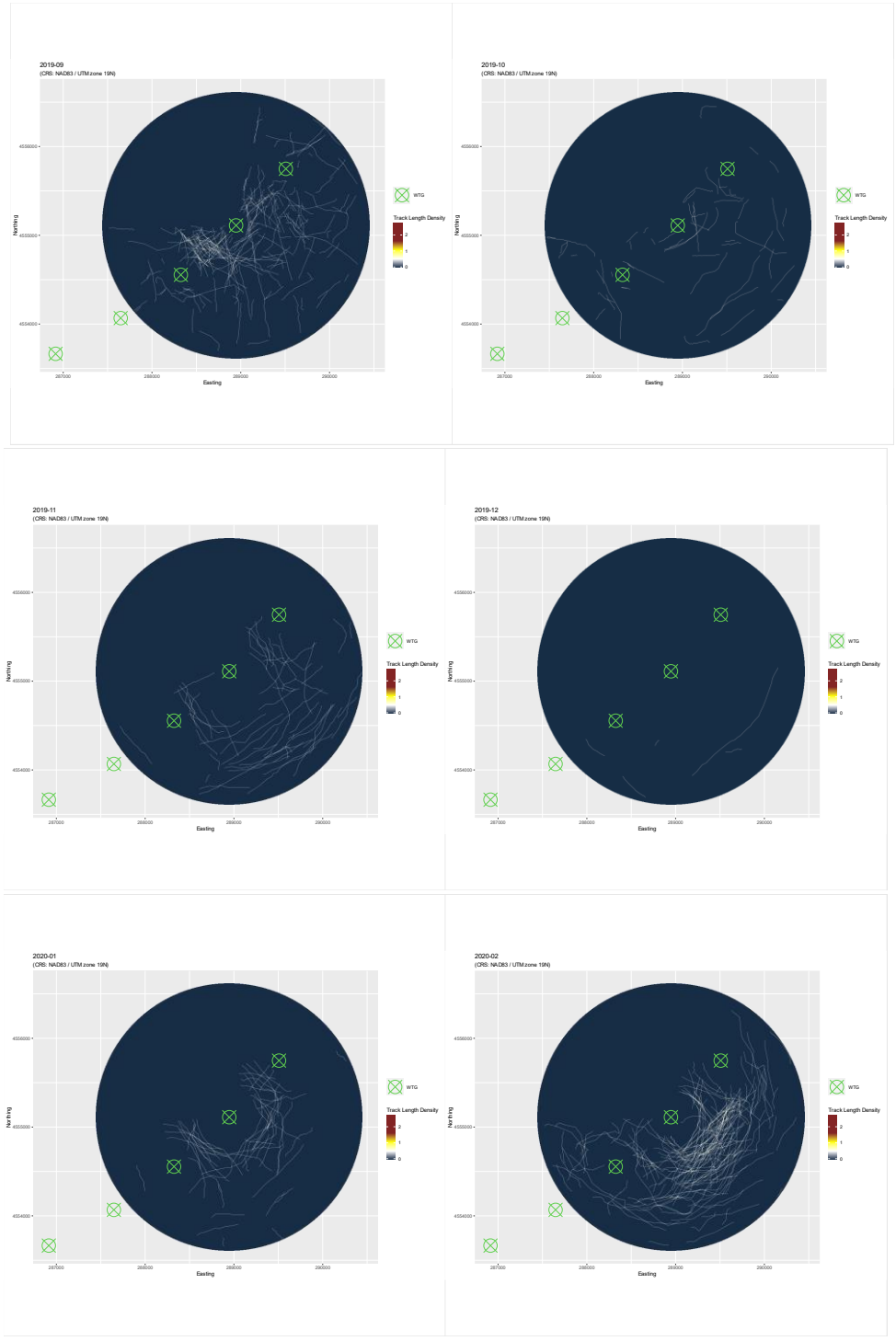

Figure 5-8 (Cont.)

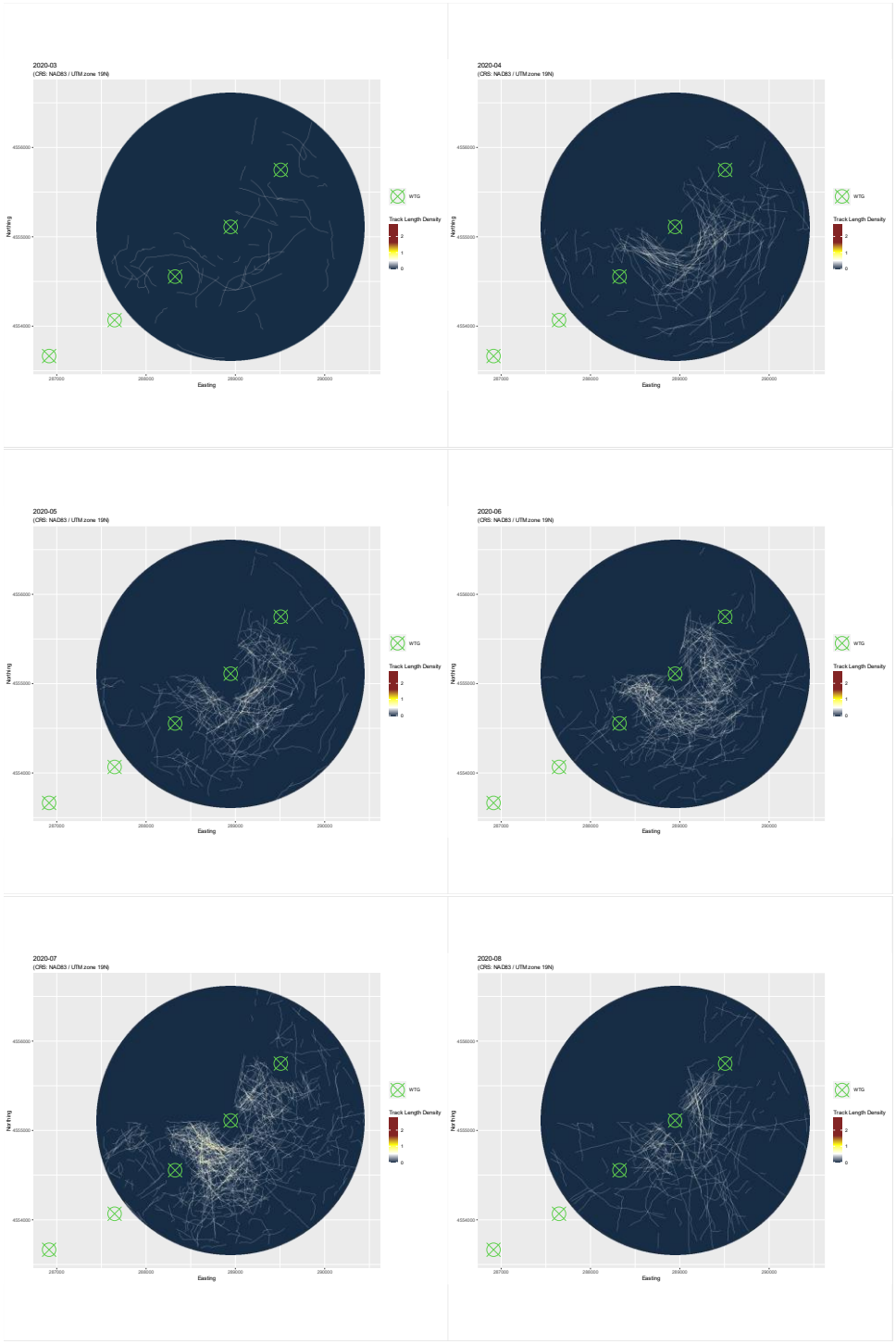

Figure 5-9 (Cont.)

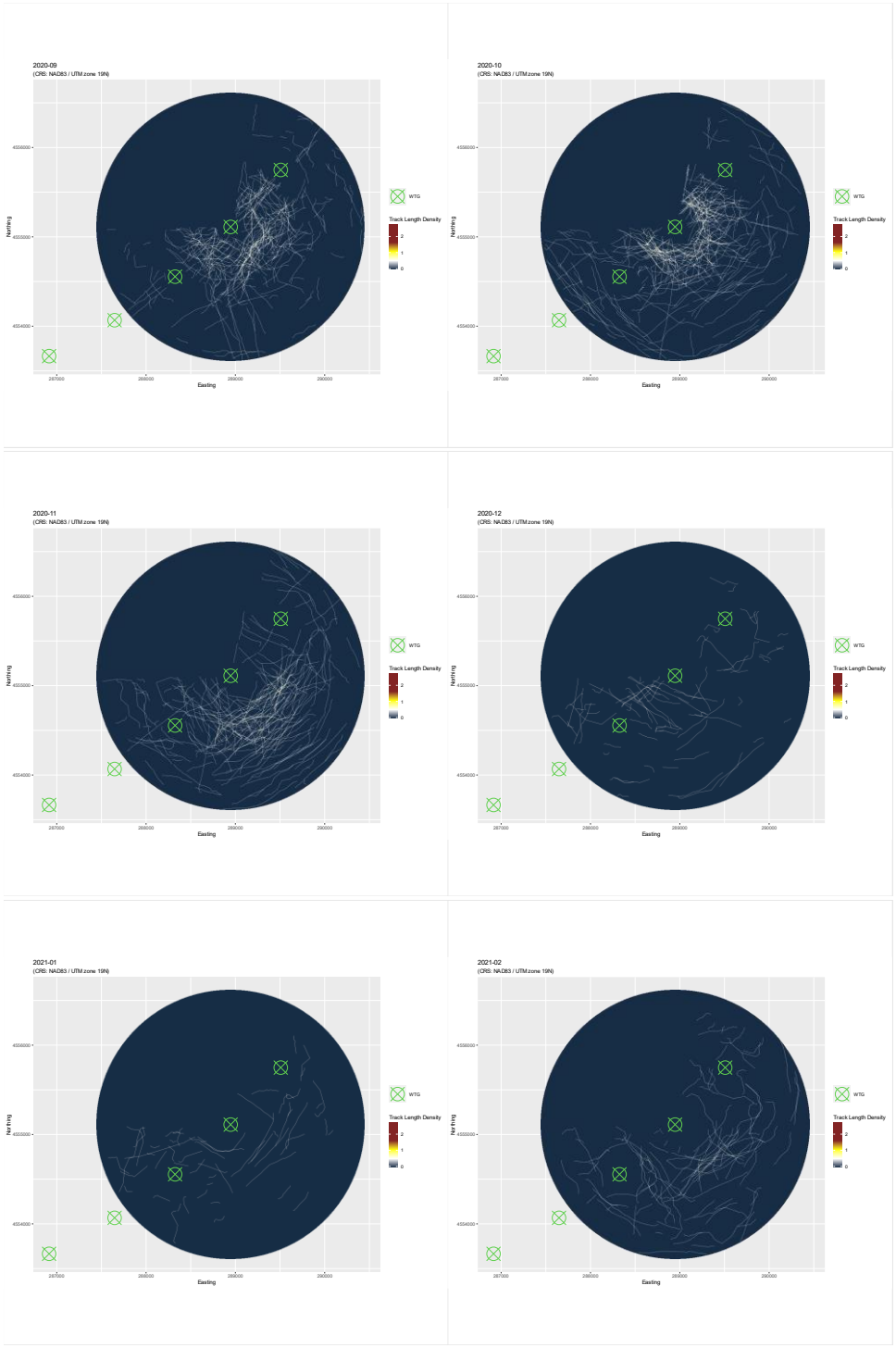

Figure 5-10 (Cont.)

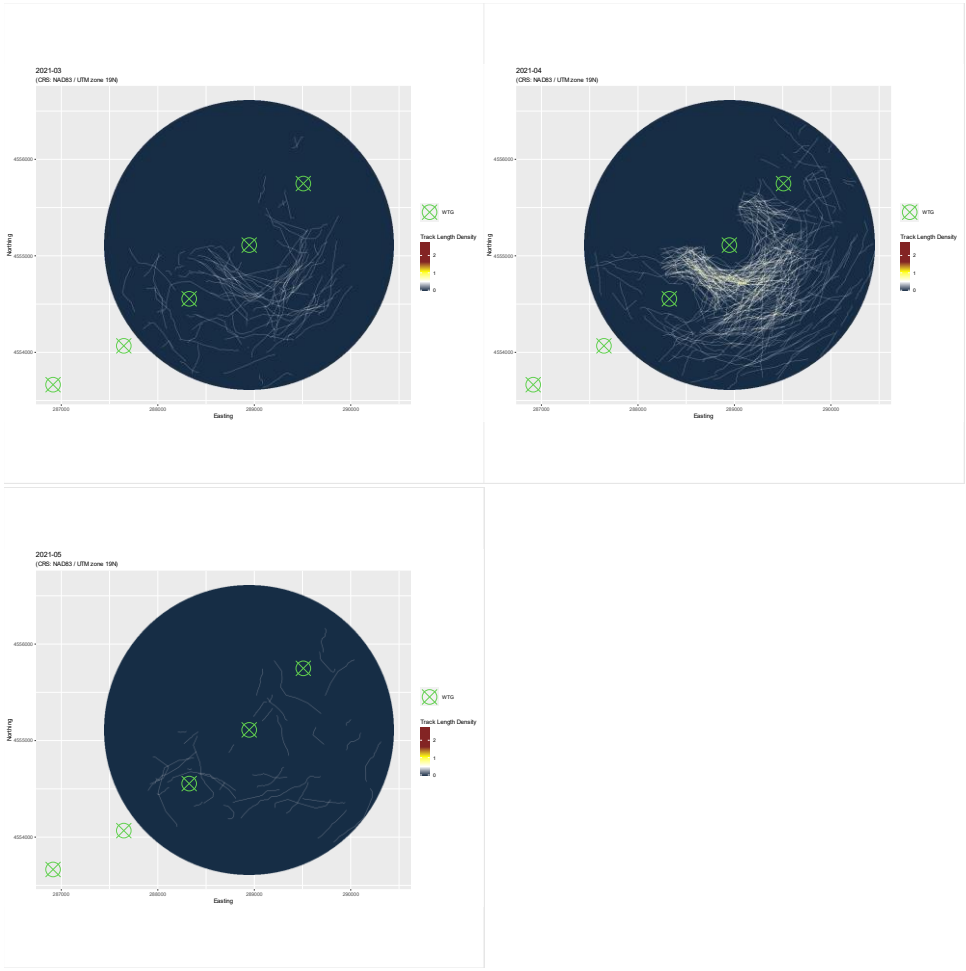

Figure 5-11 (Cont.)

5.2.1 Nighttime

A monthly breakdown of the spatial distribution and density of recorded bird tracks during night hours is shown in Figure 5-12. The recorded patterns of flight distributions in all months are similar to the patterns recorded during daylight hours, clearly indicating avoidance of the turbines. Despite similar general patterns a larger number of flights are noted to enter the zones close to turbine 1 and 3 (100 m from the tip of the blades) as compared to daylight hours. The zone of avoidance still stretches from 75 m from the turbine to at least to 1/3 of the inter-turbine distance during night and like during the day a zone of higher densities is located between the turbines and 300-400 m distance along the array.

Compared to the daylight hours the fine-scale distributions of tracks during night hours display more linear patterns and N-S directions along the side of the array, possibly associated with nighttime migration along the eastern coastline of the US. This compared to daylight hours, which showed more of a tendency to circular movements around turbines 1 and 3, possibly associated with birds moving offshore and onshore during breeding season and winter foraging activities.

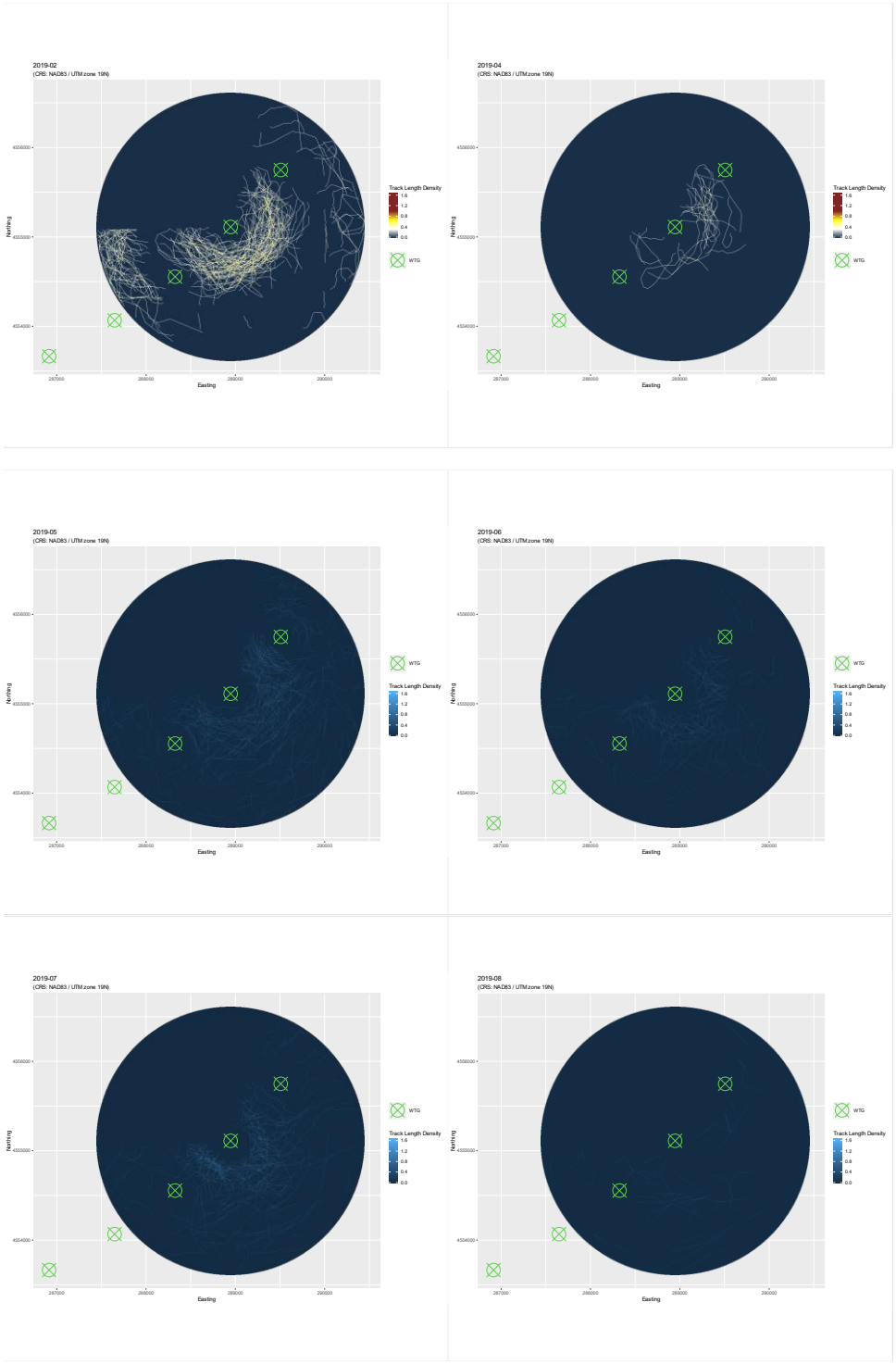

Figure 5-12 Monthly track length density patterns recorded during night hours by the radar during the period January 2019 – May 2021. The masked areas of the rotor-swept zones are marked by green circles.

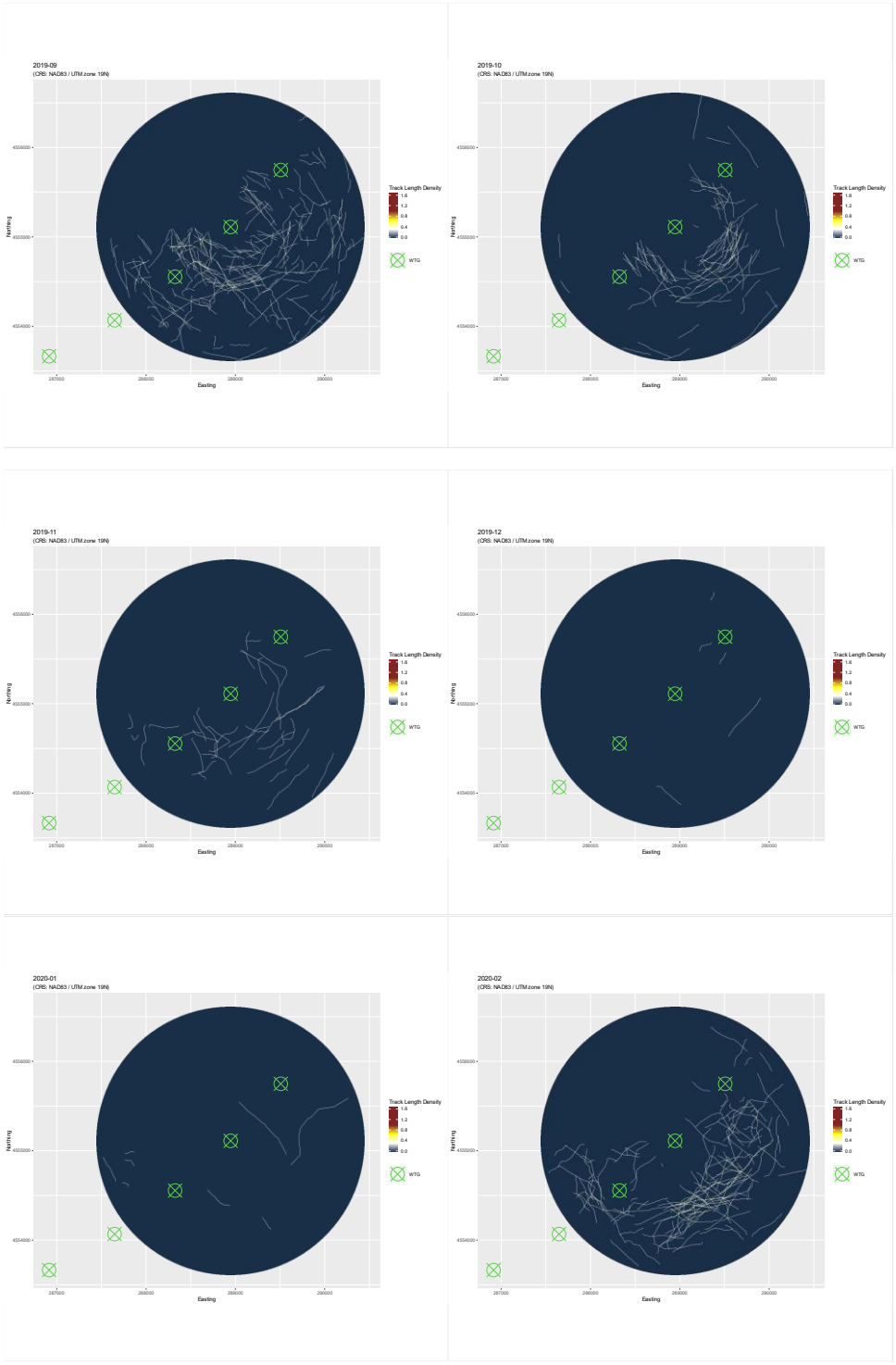

Figure 5-12 (Cont.)

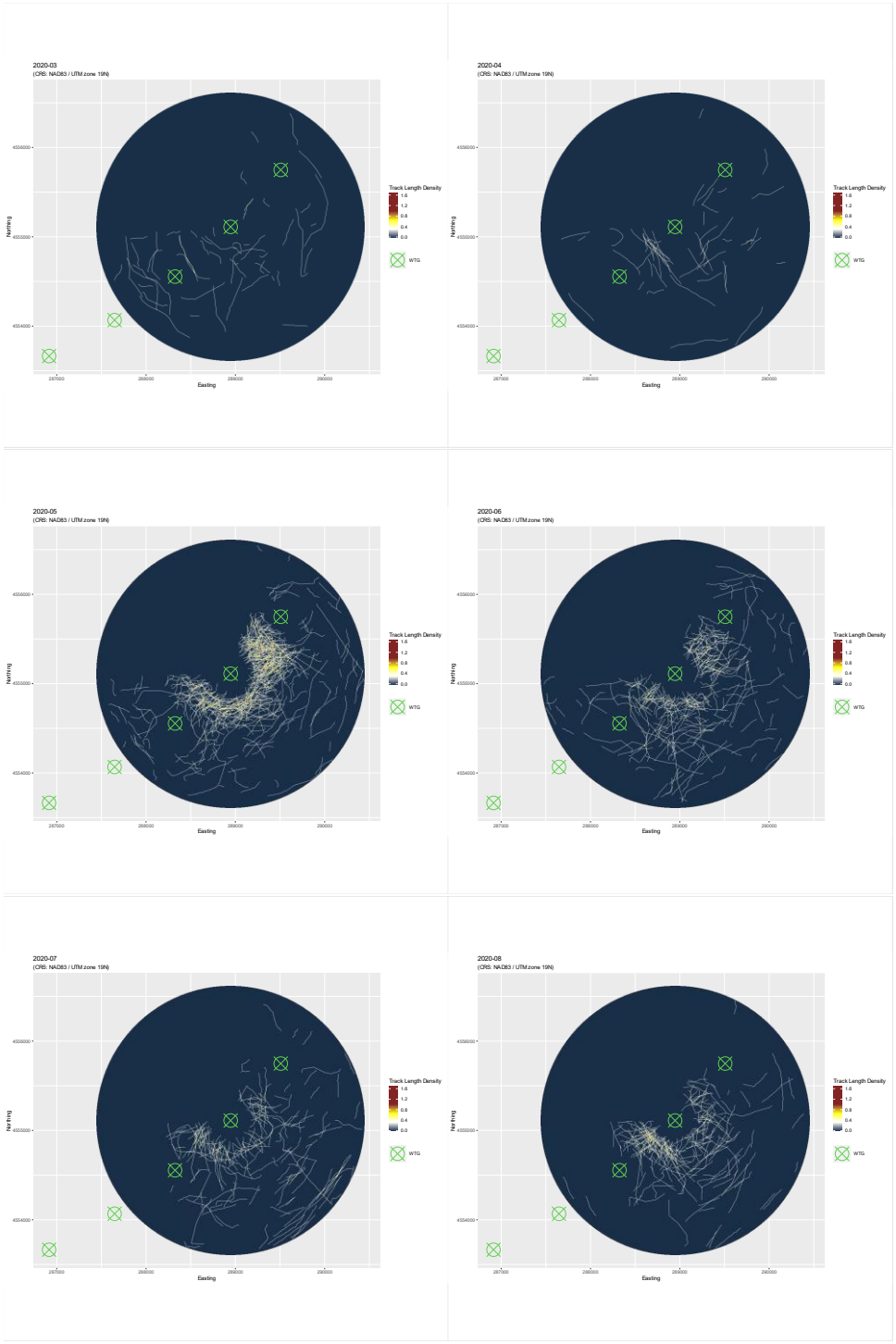

Figure 5-12 (Cont.)

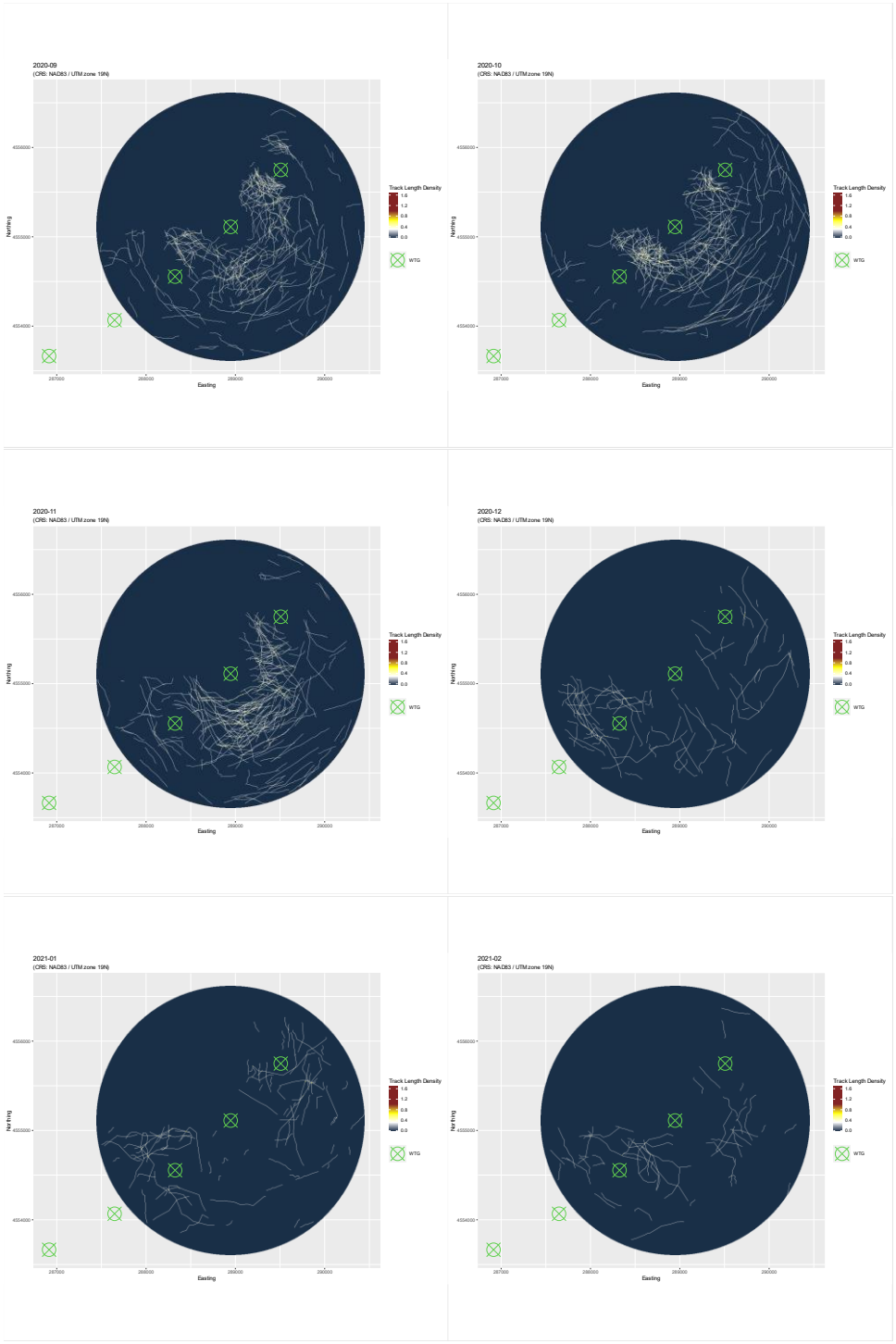

Figure 5-12 (Cont.)

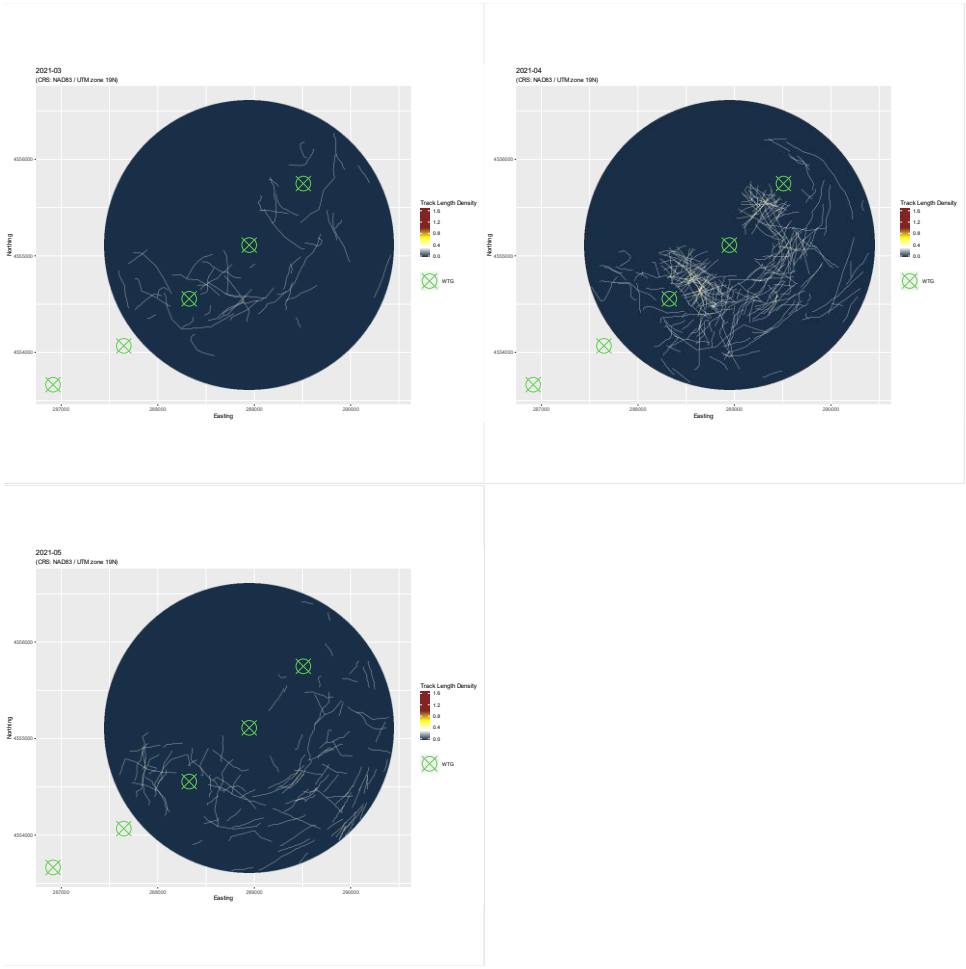

Figure 5-12 (Cont.)

5.3 Dynamics of recorded flight directions

5.3.1 General patterns

The general patterns of recorded flight directions by the radar are depicted by monthly histograms for day/night in Figure 5-13 and Figure 5-14. The histograms corroborate the findings from the analyses of spatial distributions of tracks that movements during winter and summer months at BIF are quite omni-directional. Movements during the periods of seasonal migration of birds from the northern Hemisphere, i.e., April-May and September-November are directional and show the expected dominance of movements towards NE during spring and towards SW during fall.

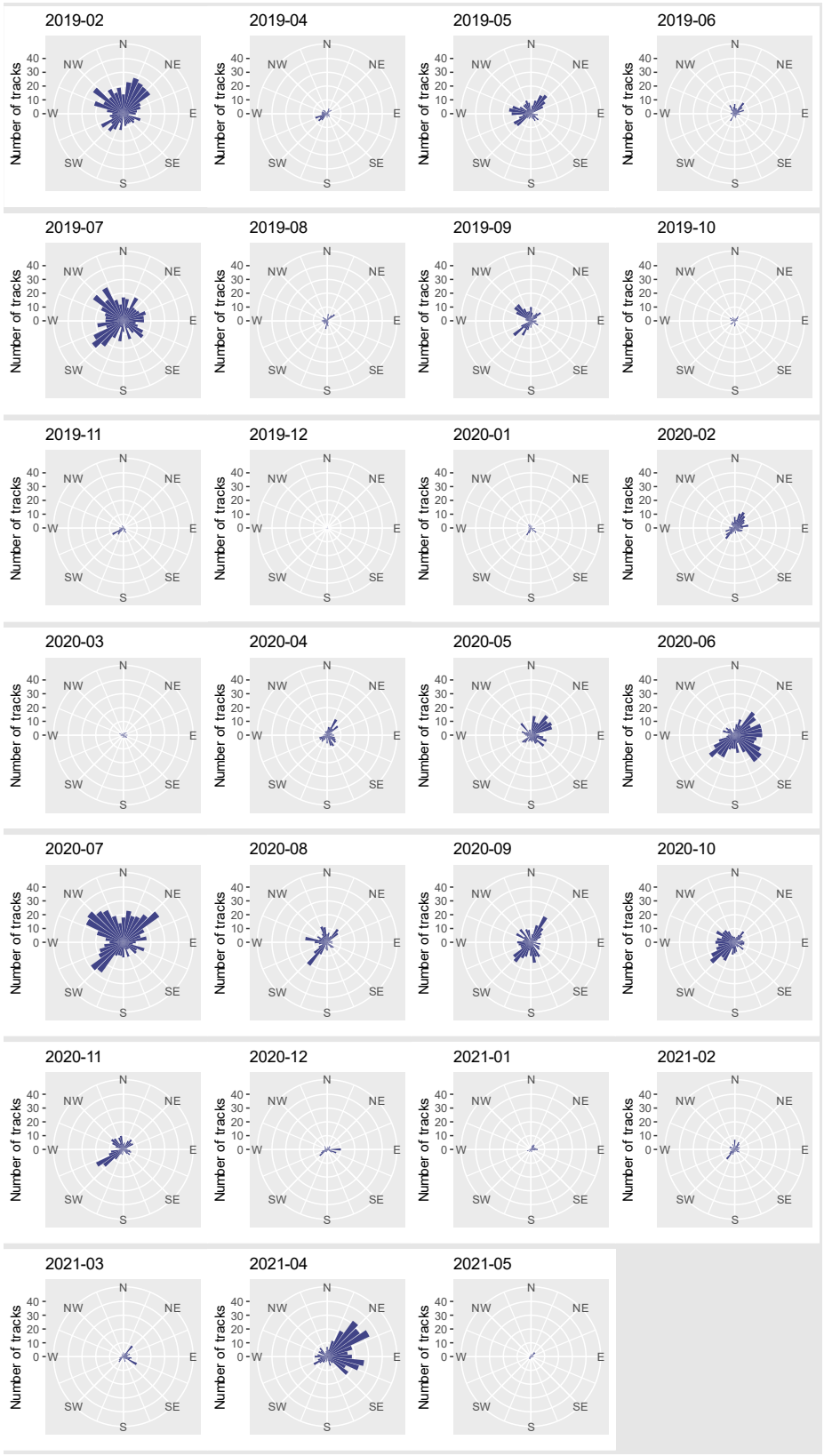

Figure 5-13 Directional histograms showing the monthly flight directions during daylight hours extracted from the radar bird tracks for the period January 2019 – May 2021. Each map represents Year-Month.

Figure 5-14 Directional histograms showing the monthly flight directions during night hours extracted from the radar bird tracks for the period January 2019 – May 2021. Each map represents Year-Month.

5.3.1 Local patterns

To assess the influence of the apparent meso avoidance behaviour on bird flight directions, monthly mean local flight directions were extracted from the radar data (Figure 5-15). The visualised local directions indicate avoidance behaviour in the zones at close distance to the turbines. This is particularly the case during the migration months of April, May, October and November when changes in the general NE/SW direction of birds is observed in between the turbines both during daytime and nighttime.

During spring migration, it seems that the responsive movement of the birds when approaching the turbines is manifested as a funnelling effect at turbine 3 and as a more marked avoidance effect at turbine 1. The reverse situation is seen during the period of fall migration when a funnelling effect seems evident at turbine 1 and a marked avoidance effect at turbine 3.

Figure 5-15 Monthly mean local flight directions extracted from the radar bird tracks for the period January 2019 – May 2021. The masked areas of the rotor-swept zones are marked by green circles.

Figure 5-15 (Cont.)

Figure 5-15 (Cont.)

Figure 5-15 (Cont.)

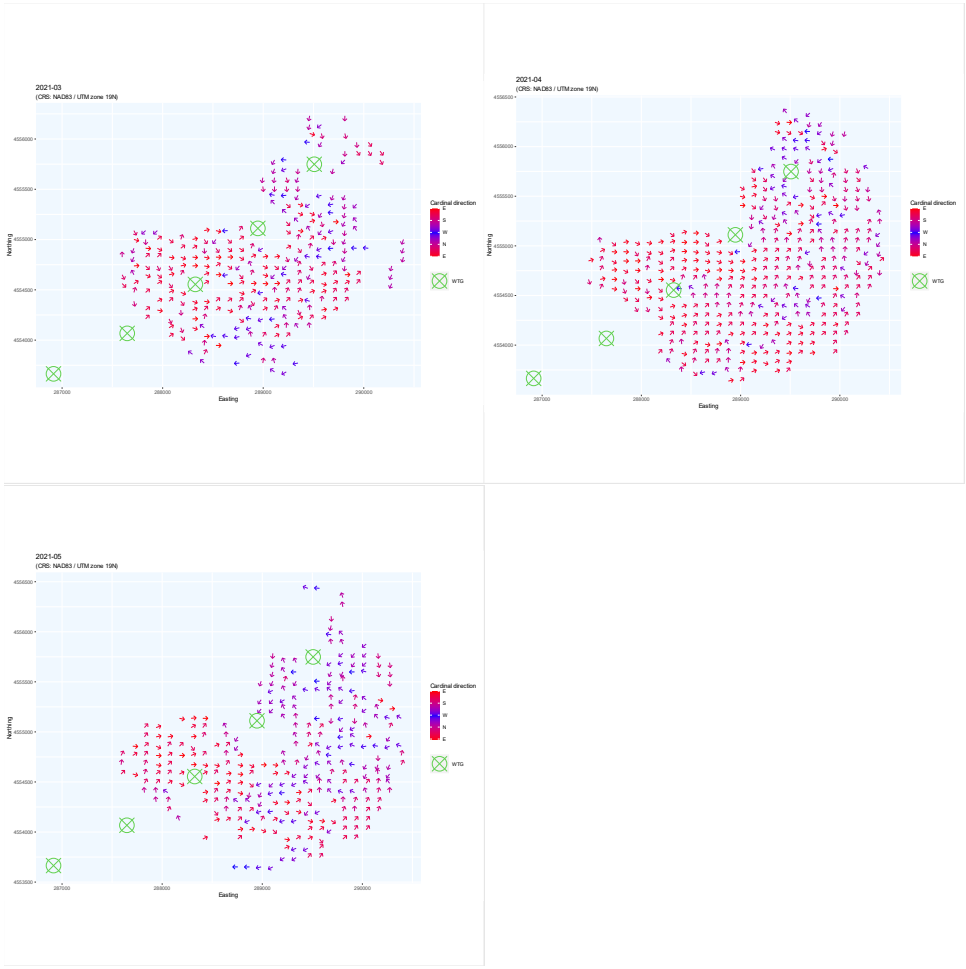

Figure 5-15 (Cont.)

5.4 Avoidance behaviour

A more generalized assessment of the profiles of avoidance as measured by the recorded bird density as a function of the distance to turbine 1 and 3 is shown in Figure 5-16 and Figure 5-17, respectively. The monthly plots confirm the impression of a reduction in bird density at 300-400 m distance from the two turbines. This pattern is most clear during the months with high bird activity. At closer inspection the deflection of birds seems to start at 300 m distance from turbine 1 and at 350 m distance from turbine 3.

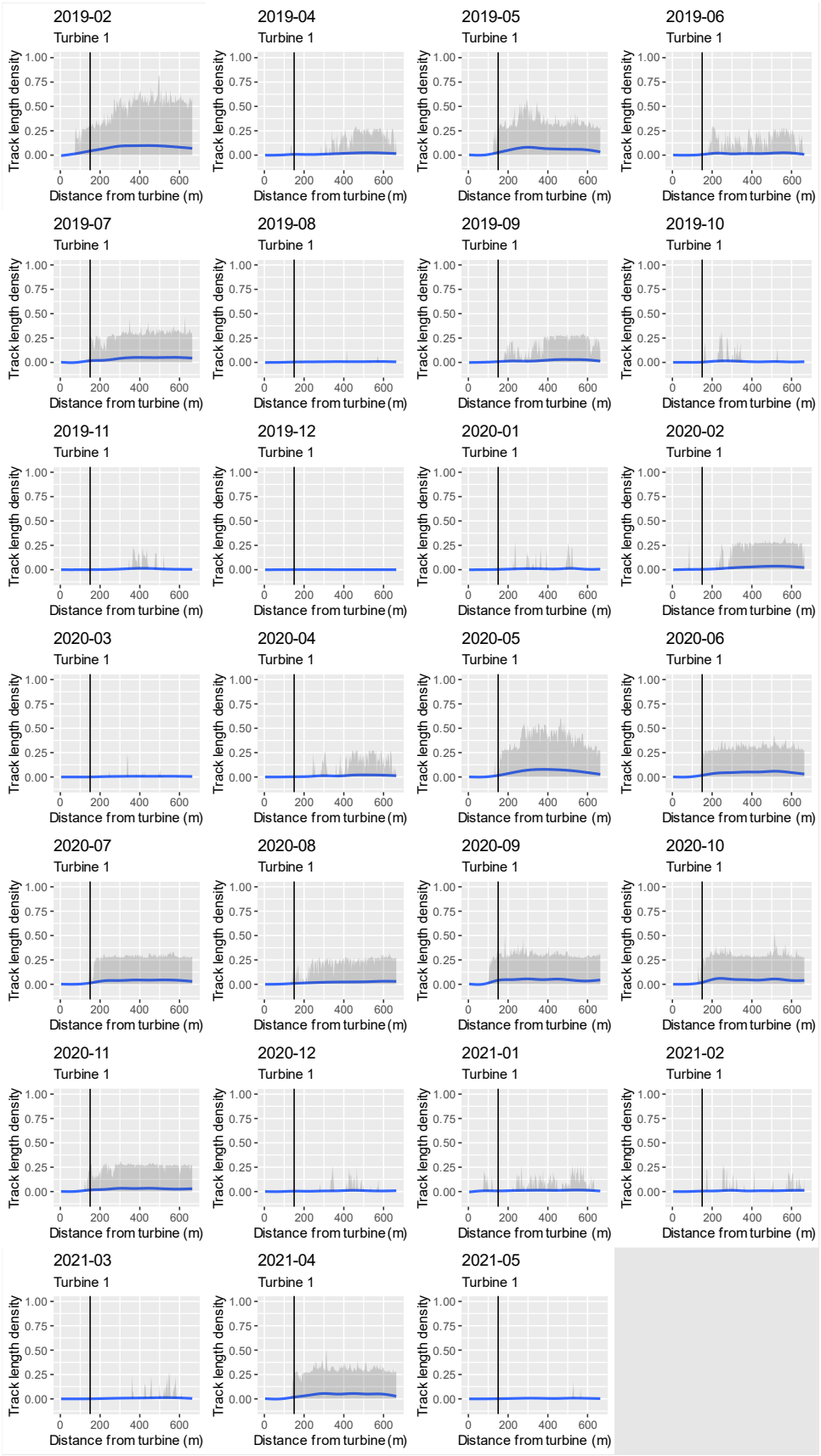

Figure 5-16 Mean monthly profiles of track length densities recorded by the radar as a function of distance to turbine 1 (m). The overall variation of the density profile at different angles around the turbine is indicated by grey bars. Vertical line depicts the

masked area within which there was insufficient radar coverage.

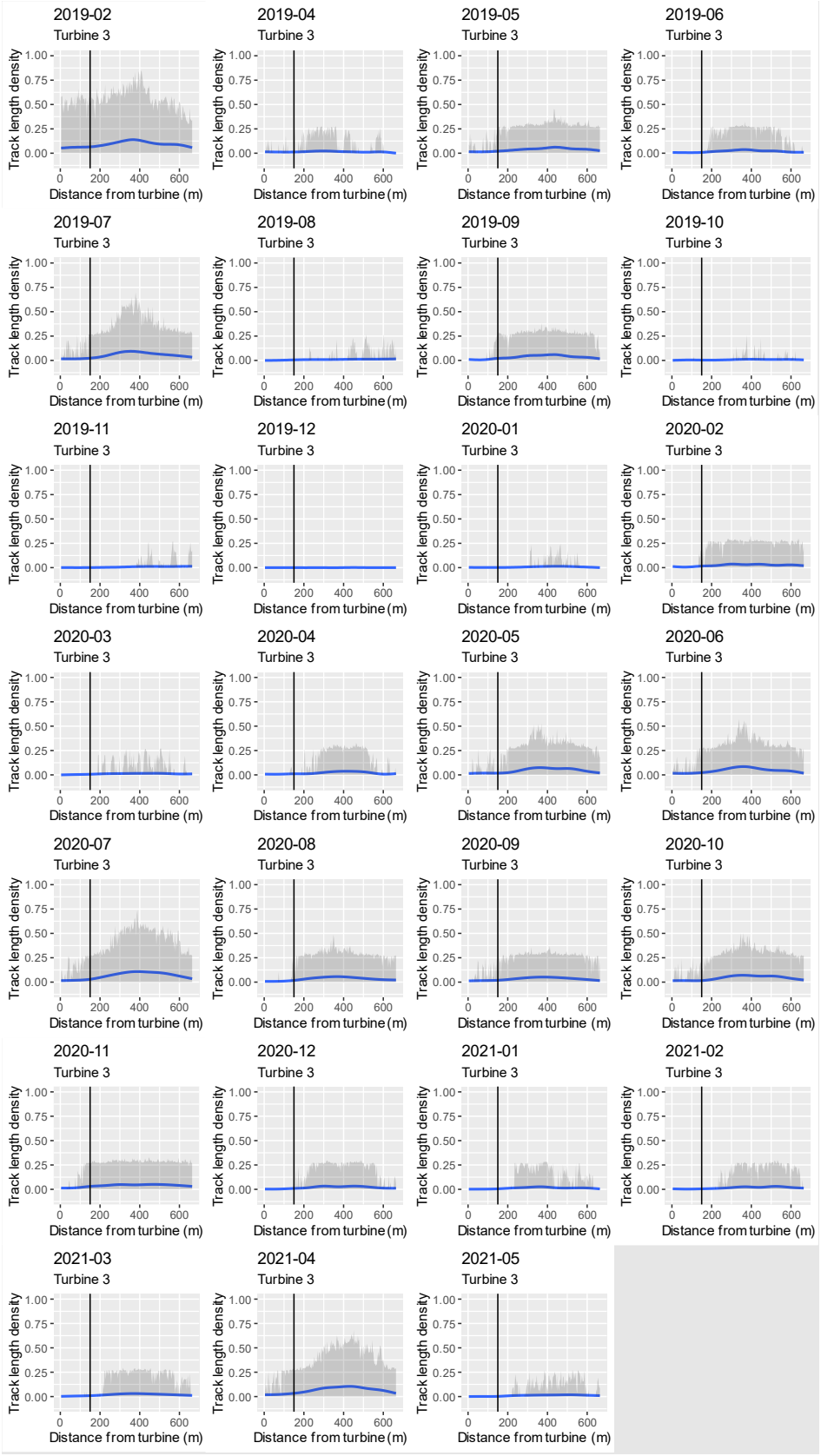

Figure 5-17 Mean monthly profiles of track length densities recorded by the radar as a function of distance to turbine 3 (m). The overall variation of the density profile at different angles around the turbine is indicated by grey bars. Vertical line depicts the masked area within which there was insufficient radar coverage.

5.5 Micro avoidance and collisions

The analysis of micro avoidance (behavior response to avoid approaching within 10 m of the turbine rotor) included a summary of video files recorded within approximately 100 m of Turbines 1 and 3.

Table 6-1 summarizes the video camera recordings that were associated with the recorded radar tracks within 100 m of Turbines 1 or 3 from August 1, 2018, to May 13, 2020; note that not all radar tracks had associated video recordings. Videos were predominantly recorded during daytime (n = 25), while only one video was recorded during nighttime.

The video recordings associated with radar tracks during the August 2018 to May 2021 study period captured images of large gulls, a potential raptor species and unidentified birds. With the exception of two incidents when gulls were recorded at 50 m distance during situations when the rotor was either still or idle, the closest distance that targets approached Turbines 1 or 3 was approximately 60 m (197 ft) from the rotor. That is to say, none of these tracks are considered to be near-misses, as in all cases the birds appeared to stay far enough from the moving blades to avoid the need for a last-second alteration in flight behavior to avoid collision. Additionally, there were no collision events detected by the camera during the August 2018 to May 2021 study period. However, due to the masking effect on the radar, it is possible that micro avoidance and/or collision events were missed in those areas not visible by the radar.

6 Conclusions

The phenology of the MUSE data showed peak densities during the daylight hours of the summer months dominated by Great and Cory's shearwater with a second peak during winter dominated by Herring gull. The diurnal patterns of activity documented highest densities during dawn hours. The recorded patterns of track density distributions during both daylight and night hours in all months clearly indicated avoidance of the turbines. This was so, even if the radar was shaded within the nearest 75 m from the turbine tower due to the static clutter induced by the turbine and rotor blades. The zone of avoidance seemed to stretch at least to 1/3 of the inter-turbine distance equivalent to 275 m. The general avoidance behavior also clearly translated into a zone of higher densities located between the turbines and at 300-400 m distance along the array; that is, close to the mid-point between adjacent pairs of turbines. Fine-scale flight distributions of tracks displayed more linear patterns along the side of the array during the night than during daytime, possibly associated with nighttime migration along the eastern coastline of Rhode Island. During daylight hours, radar tracks showed more of a tendency to circular patterns around turbines 1 and 3, possibly associated with birds moving offshore and onshore during breeding season and winter foraging activities. Flight directions recorded by the radar corroborated the finding that movements during winter and summer months were less directional than during the periods of seasonal migration. Although these general spatio-temporal trends are obvious from the high-resolution graphics and plots it is recommended to undertake formal statistical tests of these trends, including tests of the influence of weather (wind) conditions on the variation of avoidance behaviour at BIWF.

With the exception of two incidents when gulls were recorded at 50 m distance during situations when the rotor was either still or idle, the closest distance that targets approached Turbines 1 or 3 was approximately 60 m (197 ft) from the rotor. Accordingly, none of these tracks are considered to be near-misses, as in all cases the birds appeared to stay far enough from the moving blades to avoid the need for a last-second alteration in flight behavior to avoid collision. Additionally, there were no collision events detected by the camera during the August 2018 to May 2021 study period.

Table 6-1 Summary of video camera recordings associated with radar tracks or points within 100 m of Turbines 1 or 3, August 1, 2018, to May 16, 2020.

Date	Season	Time (local)	Time of Day	Flight Direction	Closest Distance from Nearest Turbine	Nearest Turbine	Species (Notes)
9/20/2018	Late-Summer/Fall 2018	23:25	nighttime	SW	113	1	large gull
10/3/2018	Late-Summer/Fall 2018	13:49	daytime	multiple	multiple	1	large gull
10/3/2018	Late-Summer/Fall 2018	14:00	daytime	NNW	131	1	large gull
11/18/2018	Winter 2018/2019	12:11	daytime	WSW	106	1	large gull
11/18/2018	Winter 2018/2019	14:09	daytime	WNW	70	1	unidentified bird
11/18/2018	Winter 2018/2019	14:32	daytime	N	86	1	large gull
11/17/2018	Winter 2018/2019	15:10	daytime	NNW	103	3	large gull
11/19/2018	Winter 2018/2019	8:47	daytime	W	78	3	large gull

Date	Season	Time (local)	Time of Day	Flight Direction	Distance from Nearest Turbine	Nearest Turbine	Species (Notes)
11/19/2018	Winter 2018/2019	10:46	daytime	S	106	3	large gull
11/19/2018	Winter 2018/2019	10:59	daytime	E	103	3	large gull
12/5/2018	Winter 2018/2019	12:47	daytime	SW	107	3	possible raptor
1/12/2019	Winter 2018/2019	14:36	daytime	N	111	3	unidentified bird
5/8/2019	Summer 2019	11:56	daytime	na	73	1	unidentified bird
7/12/2019	Summer 2019	20:13	daytime	na	85	3	large gull
10/24/2019	Autumn 2019	07:25	daytime	SW	75	3	Large gull
11/06/2019	Autumn 2019	10:55	daytime	SW	100	3	Large gull
11/19/2019	Autumn 2019	13:13	daytime	N	100	3	Herring gull

Date	Season	Time (local)	Time of Day	Flight Direction	Distance from Nearest Turbine	Nearest Turbine	Species (Notes)
01/29/2020	Winter 2020	16:08	Daytime	N	80	3	Large gull
01/31/2020	Winter 2020	06:55	Daytime	NW	90	3	Large gull, rotor still
01/31/2020	Winter 2020	07:00	Daytime	NW	100	3	Large gull, rotor still
01/31/2020	Winter 2020	07:02	Daytime	E	50	3	Large gull, rotor still
01/31/2020	Winter 2020	07:12	Daytime	E	80	3	Large gull, rotor still
03/11/2020	Spring 2020	07:24	Daytime	SE	100	3	Large gull
03/26/2020	Spring 2020	16:23	Daytime	W	90	3	Large gull
05/04/2020	Spring 2020	06:16	Daytime	E	50	3	Large gull, rotor idle
05/16/2020	Spring 2020	09:13	Daytime	SW	70	1	Herring gull

Date	Season	Time (local)	Time of Day	Flight Direction	Distance from Nearest Turbine	Nearest Turbine	Species (Notes)
05/31/2020	Spring 2020	13:29	Daytime	NW	100	3	Large gull
05/31/2020	Spring 2020	14:24	Daytime	NW	60	3	Large gull, rotor idle
05/31/2020	Spring 2020	14:41	Daytime	NW	100	3	Large gull, rotor idle
06/05/2020	Summer 2020	10:59	Daytime	NW	90	3	Large gull
06/18/2020	Summer 2020	20:07	Daytime	SW	100	1	Large gull
06/23/2020	Summer 2020	06:24	Daytime	E	90	3	Herring gull
07/29/2020	Summer 2020	08:21	Daytime	NW	100	3	Large gull, rotor still
08/13/2020	Summer 2020	17:22	Daytime	NW	100	3	Large gull
08/21/2020	Summer 2020	08:08	Daytime	SE	80	3	Large gull, flying along rotor

Date	Season	Time (local)	Time of Day	Flight Direction	Distance from Nearest Turbine	Nearest Turbine	Species (Notes)
09/15/2020	Autumn 2020	20:55	Nighttime	NW	75	3	Large gull, rotor still, flying above rotor
12/07/2020	Winter 2020	12:29	Daytime	W	70	1	Herring gull, crossing rotor without adjustments, rotor still
12/23/2020	Winter 2020	16:27	Daytime	NW	80	3	Herring gull, passing perpendicularly close to rotor, rotor still
12/27/2020	Winter 2020	12:10	Daytime	E	100	3	Large gull, circling between turbine 3 and 4 and subsequently feeding/landing
01/01/2021	Winter 2021	16:43	Daytime	NW	80	3	Large gull, flying along the plane of the rotor blades
02/10/2021	Winter 2021	11:52	Daytime	SW	100	3	Large gull, above rotor height
02/11/2021	Winter 2021	07:46	Daytime	NW	100	3	Large gull, Along rotor

Date	Season	Time (local)	Time of Day	Flight Direction	Distance from Nearest Turbine	Nearest Turbine	Species (Notes)
02/11/2021	Winter 2021	07:54	Daytime	-	100	3	Large gull, Circling
02/11/2021	Winter 2021	14:30	Daytime	-	100	3	Herring gull
02/26/2021	Winter 2021	07:21	Daytime	-	100	1	5 Large gulls, circling
02/26/2021	Winter 2021	07:29	Daytime	NW	25	3	Large gull, crosses perpendicularly, adjusts flight height before crossing near tip of blade
02/26/2021	Winter 2021	07:29	Daytime	E	90	3	Large gull
02/26/2021	Winter 2021	08:58	Daytime	-	100	3	Large gull, circling
02/26/2021	Winter 2021	12:53	Daytime	W	90	3	Herring gull, flying below rotor height
03/10/2021	Spring 2021	06:18	Daytime	SE	50	3	Large gull, deflects vertically and increases height close to tip of blade

Date	Season	Time (local)	Time of Day	Flight Direction	Distance from Nearest Turbine	Nearest Turbine	Species (Notes)
03/16/2021	Spring 2021	13:48	Daytime	W	40	3	Rotor idle, Large gull, crosses perpendicularly without changing flight
03/21/2021	Spring 2021	11:51	Daytime	W	80	3	Rotor still, Large gull, flying along plane of rotor
04/03/2021	Spring 2021	11:52	Daytime	W	100	3	3 Herring gulls
05/08/2021	Spring 2021	12:39	Daytime	W	100	1	Rotor still, Large gull
05/08/2021	Spring 2021	15:40	Daytime	W	100	1	Flies along rotor plane, Herring gull
05/08/2021	Spring 2021	15:40	Daytime	E	40	1	Flies along rotor plane, Herring gull

NOTE: The majority of radar tracks/points did not have associated video camera recordings due to operational downtime of the radar and/or camera.

7 References

van Erp, J. A., van Loon, E. E., De Groeve, J., Bradarić, M., & Shamoun-Baranes, J. (2024). A framework for post-processing bird tracks from automated tracking radar systems. Methods in Ecology and Evolution, 15(1), 130-143. https://doi.org/10.1111/2041-210X.14249

Skov, H., Heinänen, S., Norman, T., Ward, R.M., Méndez-Roldán, S. & Ellis, I. (2018). ORJIP Bird Collision and Avoidance Study. Final report – April 2018. The Carbon Trust. United Kingdom. 247 p

Appendices

Appendix A Detection probabilities and vertical coverage of FAR-3000 radar

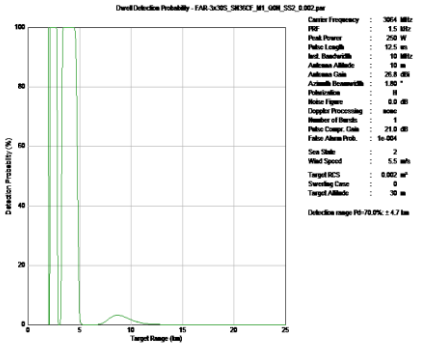

Passerine-type

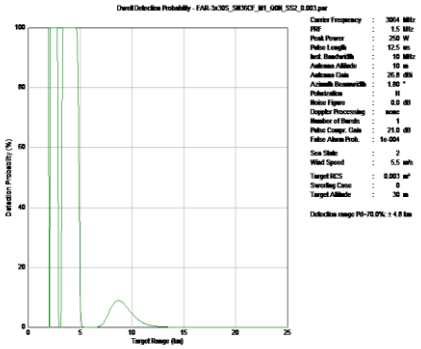

Wader-type

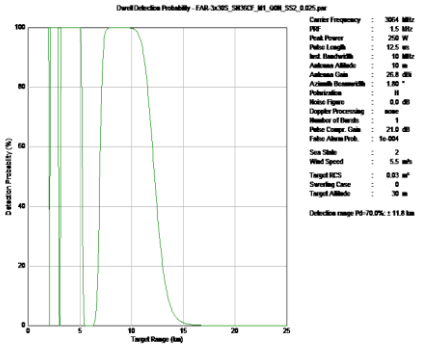

Goose-type

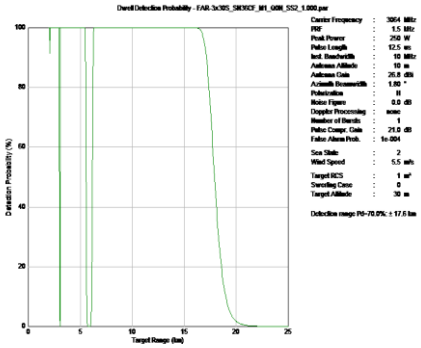

Flock of birds

Figure A1. Detection probability graphs for i) passerine-type, ii) wader-type, iii) goose-type and iv) flock of birds for FAR-3000 solid state S-band radar.

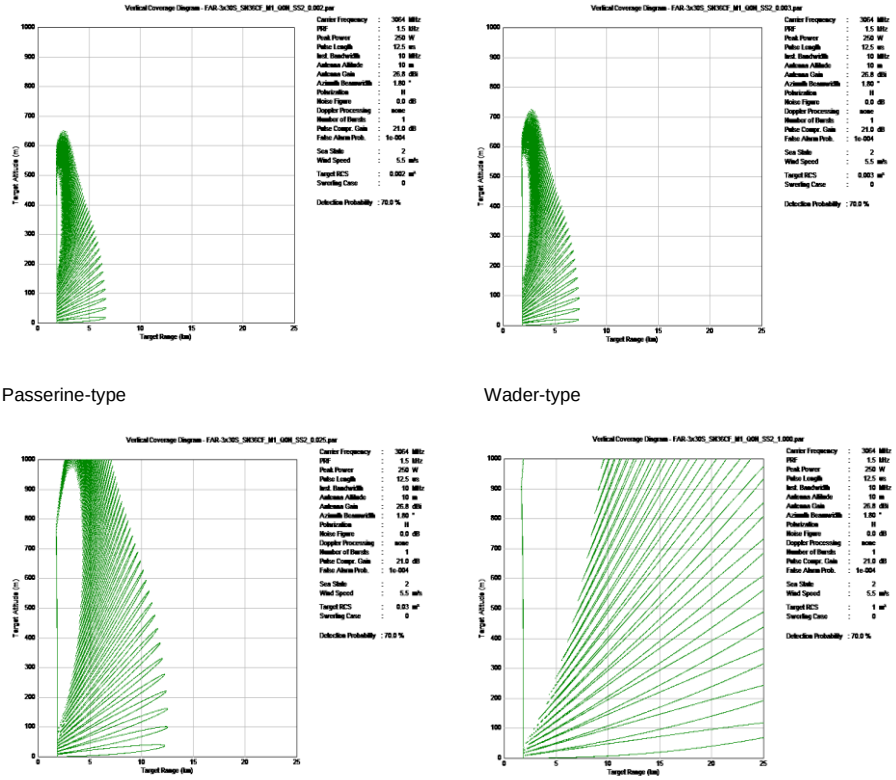

Passerine-type

Wader-type

Goose-type

Flock of birds

Figure A2. Vertical coverage graphs for i) passerine-type, ii) wader-type, iii) goose-type and iv) flock of birds for FAR-3000 solid state S-band radar.